X-Ray Burst and Persistent Emission Properties of the Magnetar SGR 1830-0645 in Outburst

The Astrophysical Journal, 924:136 (10pp), 2022 January 10 https://doi.org/10.3847/1538-4357/ac3756

X-Ray Burst and Persistent Emission Properties of the Magnetar SGR 1830-0645 in Outburst

George Younes[1,2], Chin-Ping Hu[3], Karishma Bansal[4], Paul S. Ray[5], Aaron B. Pearlman[6,7,8,25], Franz Kirsten[9], Zorawar Wadiasingh[10,11,12], Ersin Göğüş[13], Matthew G. Baring[14], Teruaki Enoto[15], Zaven Arzoumanian[16], Keith C. Gendreau[16], Chryssa Kouveliotou[1,2], Tolga Güver[17,18], Alice K. Harding[19], Walid A. Majid[4,8], Harsha Blumer[20,21], Jason W. T. Hessels[22], Marcin P. Gawroński[23], Vladislavs Bezrukovs[24], and Arturs Orbidans[24]
[1] Department of Physics, The George Washington University, Washington, DC 20052, USA; gyounes@gwu.edu
[2] Astronomy, Physics and Statistics Institute of Sciences (APSIS), The George Washington University, Washington, DC 20052, USA
[3] Department of Physics, National Changhua University of Education, Changhua 50007, Taiwan
[4] Jet Propulsion Laboratory, California Institute of Technology, Pasadena, CA 91109, USA
[5] Space Science Division, U.S. Naval Research Laboratory, Washington, DC 20375, USA
[6] Department of Physics, McGill University, 3600 rue University, Montréal, QC H3A 2T8, Canada[26]
[7] McGill Space Institute, McGill University, 3550 rue University, Montréal, QC H3A 2A7, Canada
[8] Division of Physics, Mathematics, and Astronomy, California Institute of Technology, Pasadena, CA 91125, USA
[9] Department of Space, Earth and Environment, Chalmers University of Technology, Onsala Space Observatory, SE-439 92, Onsala, Sweden
[10] Department of Astronomy, University of Maryland, College Park, MD 20742, USA
[11] Astrophysics Science Division, NASA Goddard Space Flight Center, Greenbelt, MD 20771, USA
[12] Center for Research and Exploration in Space Science and Technology, NASA/GSFC, Greenbelt, MD 20771, USA
[13] Sabancı University, Faculty of Engineering and Natural Sciences, İstanbul 34956 Turkey
[14] Department of Physics and Astronomy—MS 108, Rice University, 6100 Main Street, Houston, TX 77251-1892, USA
[15] Extreme Natural Phenomena RIKEN Hakubi Research Team, Cluster for Pioneering Research, RIKEN, 2-1 Hirosawa, Wako, Saitama 351-0198, Japan
[16] Astrophysics Science Division, NASA Goddard Space Flight Center, Greenbelt, MD 20771, USA
[17] Istanbul University, Science Faculty, Department of Astronomy and Space Sciences, Beyazıt, 34119, Istanbul, Turkey
[18] Istanbul University Observatory Research and Application Center, Istanbul University 34119, Istanbul Turkey
[19] Theoretical Division, Los Alamos National Laboratory, Los Alamos, NM 87545, USA
[20] Department of Physics and Astronomy, West Virginia University, Morgantown, WV 26506, USA
[21] Center for Gravitational Waves and Cosmology, West Virginia University, Chestnut Ridge Research Building, Morgantown, WV 26505, USA
[22] Anton Pannekoek Institute for Astronomy, University of Amsterdam, Science Park 904, 1098 XH, Amsterdam, The Netherlands, ASTRON, Netherlands Institute for Radio Astronomy, Oude Hoogeveensedijk 4, 7991 PD Dwingeloo, The Netherlands
[23] Institute of Astronomy, Faculty of Physics, Astronomy and Informatics, Nicolaus Copernicus University, Grudziadzka 5, 87-100 Toruń, Poland
[24] Engineering Research Institute Ventspils International Radio Astronomy Centre, Ventspils University of Applied Sciences, Inzenieru street 101, Ventspils, LV-3601, Latvia
Received 2021 June 15; revised 2021 October 21; accepted 2021 November 6; published 2022 January 19

Abstract

We report on NICER X-ray monitoring of the magnetar SGR 1830−0645 covering 223 days following its 2020 October outburst, as well as Chandra and radio observations. We present the most accurate spin ephemerides of the source so far: $\nu = 0.096008680(2)$ Hz, $\dot{\nu} = -6.2(1) \times 10^{-14}$ Hz s^{-1}, and significant second and third frequency derivative terms indicative of nonnegligible timing noise. The phase-averaged 0.8–7 keV spectrum is well fit with a double-blackbody (BB) model throughout the campaign. The BB temperatures remain constant at 0.46 and 1.2 keV. The areas and flux of each component decreased by a factor of 6, initially through a steep decay trend lasting about 46 days, followed by a shallow long-term one. The pulse shape in the same energy range is initially complex, exhibiting three distinct peaks, yet with clear continuous evolution throughout the outburst toward a simpler, single-pulse shape. The rms pulsed fraction is high and increases from about 40% to 50%. We find no dependence of pulse shape or fraction on energy. These results suggest that multiple hot spots, possibly possessing temperature gradients, emerged at outburst onset and shrank as the outburst decayed. We detect 84 faint bursts with NICER, having a strong preference for occurring close to the surface emission pulse maximum—the first time this phenomenon is detected in such a large burst sample. This likely implies a very low altitude for the burst emission region and a triggering mechanism connected to the surface active zone. Finally, our radio observations at several epochs and multiple frequencies reveal no evidence of pulsed or burst-like radio emission.

Unified Astronomy Thesaurus concepts: Neutron stars (1108); Magnetars (992); Compact objects (288); Soft gamma-ray repeaters (1471)

1. Introduction

The variable emission from magnetars, spanning timescales from milliseconds to years, constitutes distinctive character that separates them from the rest of the isolated neutron star family. Magnetars emit bright, hard X-ray short bursts with luminosities ranging from 10^{37} to 10^{41} erg s^{-1} (e.g., Collazzi et al. 2015) and subsecond duration. Often accompanying these bursts, magnetars enter a period of elevated persistent flux level

[25] McGill Space Institute (MSI) Fellow.
[26] FRQNT Postdoctoral Fellow.

that could exceed their quiescent emission by as many as three orders of magnitude, i.e., outbursts (e.g., Coti Zelati et al. 2018). Historically, these properties were observed in magnetars with a narrow range of spin periods around 2–12 s and large spin-down rates $\dot{P} \sim 10^{-11}$–10^{-13} s s^{-1}. Assuming magnetic dipole braking, these timing properties imply large dipolar field strengths, typically in the range of $B \sim 10^{13} - 10^{15}$ G at the equator, and young spin-down ages of a few thousand years (e.g., Kouveliotou et al. 1998; see also Mereghetti 2008; Kaspi & Beloborodov 2017 for reviews). The large available magnetic energy is putatively the main source of power in magnetars since, for most, the rotational energy loss is incapable of powering their X-ray output in quiescence and/or during outbursts (Thompson & Duncan 1996; Thompson et al. 2002; Turolla et al. 2015).

While the aforementioned temporal characteristics are certainly representative of the bulk of the magnetar population, magnetar-like activity has now been observed from several other classes of isolated neutron stars: low B-field magnetars, e.g., SGR 0418+5729 ($B \sim 6 \times 10^{12}$ G; Rea et al. 2013), high B-field rotationally powered pulsars (PSR J1846−0258 and PSR J1119−6127; Gavriil et al. 2008; Archibald et al. 2016; Göğüş et al. 2016), and a central compact object with a very long spin period of about 6.67 hr (Rea et al. 2016). Moreover, a wind nebula, an otherwise common characteristic of young rotation-powered pulsars, has been detected around a typical magnetar, Swift J1834.9−0846 (Younes et al. 2016). These results strengthen the case for a connection, perhaps evolutionary, among all isolated neutron stars (Viganò et al. 2013).

On 2020 October 10, the BAT instrument on board the Neil Gehrels Swift Observatory (Swift) triggered on a short, soft gamma-ray burst from the direction of the Galactic plane, and prompt XRT observations revealed a bright, previously unknown X-ray source, now dubbed SGR 1830−0645 (Page et al. 2020). Using the same data set, Göğüş et al. (2020) reported the detection of coherent pulsations with a spin period of 10.4 s, confirmed with NICER a few hours later (Younes et al. 2020b). NICER performed intense monitoring of the source in the ensuing days and subsequently (11 days later) revealed the detection of a spin-down rate, $\dot{\nu} \approx 9.0 \times 10^{-14}$ Hz s^{-1}, flux decay, and the detection of numerous short X-ray bursts (Ray et al. 2020). All of these characteristics fall within the realm of typical magnetar properties, implying that SGR 1830−0645 is a new addition to the magnetar family (see also Coti Zelati et al. 2021). So far, the source has not been detected in radio at several frequencies (Maan et al. 2020; Surnis et al. 2020; Coti Zelati et al. 2021).

In this paper, we present the detailed soft X-ray and radio properties of SGR 1830−0645 following its first-detected outburst utilizing the NICER X-ray telescope, Chandra telescope, and several radio facilities. We introduce our observations and data reductions in Section 2. Our results are presented in Section 3. We discuss the implications of our findings in Section 4, including our assumed fiducial distance of 4 kpc to the source.

2. Observations and Data Reduction

2.1. X-Rays

We observed SGR 1830−0645 with NICER starting approximately 4 hr after its discovery with BAT on 2020 October 10 at 14:29 UTC (Page et al. 2020). Prior to the Sun-constrained period that started on 2020 November 17, 37 observations were carried out (ObsIDs 3201810101 to 3201810137). We restarted the NICER campaign on 2021 February 10. Our current analysis includes data extending up to 2021 May 21 (up to ObsID 4201810118). NICER consists of 56 co-aligned X-ray concentrating optics covering a 30 arcmin^2 field of view and providing a collecting area of 1900 cm^2 at 1.5 keV. It offers high-precision timing and spectral capabilities, while affording a low background (Gendreau et al. 2016). We processed NICER data using `NICERDAS` version v007a, as part of HEASOFT version 6.27.2. Good time intervals were created from raw level 1 event files using the NICER tool `nicerl2`. We use the default filtering criteria as described in the NICER Data Analysis Guide,[27] except the underonly_range has been relaxed to 0–300. This background is mainly due to optical loading and only affects the low-energy part of the spectrum, below the 0.8–7 keV range we consider for all of our analyses. This choice for the energy range is driven by the hydrogen column density in the direction of the source and its soft spectrum. We extracted background spectra utilizing the `nibackgen3C50` method (Remillard et al. 2021) and added a conservative 20% systematic uncertainty to the estimated background number counts per NICER energy channel.

We observed the field of SGR 1830−0645 with the Chandra X-Ray Observatory Advanced CCD Imaging Spectrometer (ACIS; Garmire et al. 2003) for 4.6 ks on 2020 October 13 (ObsID 24841). The target was positioned at the nominal aim point of the S3 chip of the ACIS-S detectors. The observation was operated in 1/8 subarray mode, which provided a temporal resolution of 0.4 s. We reduced the data using the Chandra Interactive Analysis of Observations (CIAO[28] version 4.12) and the calibration database of Chandra CALDB version 4.9.2.1.

We utilize Xspec v12.11.0 (Arnaud 1996) for the NICER X-ray spectral analysis. We do not attempt any spectral analysis of the Chandra data owing to heavy pileup. We use the latest NICER response and ancillary files in the CALDB release `xti20200722`. We group the data to have 50 counts per energy bin and utilize the χ^2 statistics for model parameter estimation and error calculation. We quote all errors at the 1σ (68% uncertainty) level unless otherwise noted.

2.2. Radio Campaigns

European stations. Between 2020 October 11 and 2021 February 04, we observed SGR 1830−0645 for a total of 68.2 hr (nonoverlapping) with several European stations that are also part of the European VLBI[29] Network (EVN). The stations involved and the frequencies covered varied between observations as summarized in Table 1. Several stations observed simultaneously at complementary frequencies in an effort to cover as large a bandwidth as possible. At each participating station we recorded the raw voltage data in VLBI Data Interchange Format (VDIF; Whitney et al. 2010) with the local VLBI back ends (DBBC2). Each station recorded dual-polarization (circular) 2-bit data, which were subsequently transferred to Onsala Space Observatory for processing. We used the same pipeline as outlined in Kirsten et al. (2021),

[27] https://heasarc.gsfc.nasa.gov/docs/nicer/data_aalysis/nicer_analysis_guide.html
[28] https://cxc.cfa.harvard.edu/ciao/
[29] Very Long Baseline Interferometry.

Table 1
Summary of the Radio Observations of SGR 1830−0645 with EVN Dishes

Station[a]	Band[b]	Bandwidth (MHz)[c]	SEFD (Jy)[d]	Fluence Limits (Jy ms)[e]	Time Observed (hr)
Wb	P	60	2100	65	34.0
O8	L	100	350	8	46.9
Tr	C	250	260	4	3.4
Nt	L	230	740	12	2.0
Mc	C	240	170	3	2.0
Ir	L	100	700	17	18.0
Ib	C, X	250, 250	620, 650	10, 10	11.75, 8.60
Total telescope time/total time on source (hr)[f]					126.6, 68.2

Notes.
[a] Wb: Westerbork RT1; O8: Onsala 25 m; Tr: Toruń; Nt: Noto 32 m; Mc: Medicina 32 m; Ir: Irbene 32 m; Ib: Irbene 16 m.
[b] P: 300–364 MHz; L: 1336–1720 MHz; C(Mc,Ib): 4798–5310 MHz; C(Tr): 6500–6756 MHz; X: 8287–8543 MHz.
[c] Effective bandwidth accounting for RFI and band edges.
[d] From the http://old.evlbi.org/user_guide/EVNstatus.txt EVN status page. SEFD refers to system equivalent flux density.
[e] Assuming a 7σ detection threshold.
[f] Total time on source accounts for overlap between the participating stations.

which creates total intensity filter banks. Depending on observing frequency, the time and frequency resolution of the filter banks are in the range of 64–1024 μs and 7.812–2000 kHz, respectively.

Deep Space Network. The Deep Space Network (DSN; Pearlman et al. 2019) is a worldwide array of radio telescopes that are primarily used for spacecraft communication. The DSN radio telescopes are located at three main sites (Canberra, Australia; Goldstone, California; and Madrid, Spain), which each host a steerable 70 m radio antenna and several smaller 34 m radio dishes. When these radio telescopes are not being utilized to communicate with spacecraft, they can be used to perform radio observations of magnetars, high magnetic field pulsars, and fast radio burst (FRB) sources (see, e.g., Majid et al. 2017; Pearlman et al. 2018; Majid et al. 2020; Pearlman et al. 2020b, 2020c).

We performed a continuous radio observation of SGR 1830-0645 using the Deep Space Network (DSN) 34 m diameter radio telescope (DSS-34), located at the Canberra Deep Space Communications Complex (CDSCC) in Tidbinbilla, Australia, for 5.15 hr starting at 2020 October 12 07:00:01 UTC. The pulsar back end was used to simultaneously record data at S band (center frequency: 2.2 GHz; bandwidth: 118 MHz) and X band (center frequency: 8.3 GHz; bandwidth: 441 MHz). Power spectral density measurements at both frequency bands were channelized and saved in digital polyphase filter banks with a frequency and time resolution of 1 MHz and 512 μs, respectively. Initial results from this radio observation were presented in Pearlman et al. (2020a).

Green Bank Telescope. The 100 m Robert C. Byrd Green Bank Telescope (GBT) observed SGR 1830−0645 for 92 minutes at S band (center frequency: 2.0 GHz; bandwidth: 800 MHz) and for 90 minutes at C band (center frequency: 6.0 GHz; bandwidth: 1500 MHz) on 2020 October 13, for a total exposure of 182 minutes using the Versatile GBT Astronomical Spectrometer (VEGAS) pulsar back end in incoherent dedispersion and total intensity mode. The S- and C-band data were recorded using 4096 and 3072 frequency channels with a sampling time of 81.92 μs and 43.69 μs, respectively. The data were analyzed using the `PRESTO`[30] software package.

3. Results

3.1. Localization

We used our Chandra observation to derive the SGR 1830 −0645 localization. We selected all events in the 0.5–8 keV band detected with the S3 detector of ACIS-S, and we used the `wavdetect` tool of CIAO to search in the entire field for point sources whose detection significance is in excess of 5σ. The search resulted in only one bright source with a rate of 1.37 ± 0.02 counts s^{-1} at R.A., decl. of 277.673520, −6.754696 deg, respectively, which corresponds to RA, decl. of $18^{h}30^{m}41.^{s}64$, $-06°\ 45'\ 16.''9$ (J2000). We estimated the positional uncertainty by the 90% photon containment region around the source position as $0.''73$ (statistical only, with another $0.''8$ systematic uncertainty). No obvious extended emission is observed in our short Chandra exposure at the arcsecond or arcminute scales.

3.2. Timing

To develop a phase-connected timing model, we computed a set of pulse times of arrival (TOAs) from all NICER observations and fit them to a model. We compute TOAs using an unbinned maximum likelihood technique described in Ray et al. (2011). This technique uses an analytic pulse profile template in the likelihood calculation. Because the main pulse changes from double peaked early in the outburst (around MJD 59,154) to a single peak later, we used two templates. We tried several different template alignments, i.e., a single wide Gaussian, a multi-Gaussian model, and aligning the fundamental of a Fourier series fit to the pulse profile. We chose the ones where the timing residuals showed the smallest discontinuity at the switchover date. This turned out to be a single wide Gaussian, with slightly different widths for the early and late data (FWHM = 0.39 and 0.32, respectively). Using these templates, we computed TOAs for each segment of data of typical duration 400–1200 s. Using PINT (Luo et al. 2021), we fit the TOAs to a timing model of the form $\phi(t) = \phi_0 + \nu(t - t_0) + 1/2\dot{\nu}$ $(t - t_0)^2 + 1/6\ddot{\nu}(t - t_0)^3 + \ldots$, truncated at the highest significant (at the 5σ level) term, which in this case was $\ddot{\nu}$. Given the high NICER cadence, we were able to maintain phase coherence throughout our monitoring campaign. The parameters of the best-fit timing model are presented in Table 2, and the residuals are displayed in Figure 1. We find that the SGR 1830−0645 spin frequency is $\nu = 0.096008680(2)$ Hz and spin-down rate is $\dot{\nu} = -6.2(1) \times 10^{-14}$ Hz s^{-1}, which imply a dipole field strength at the equator $B \approx 2.7 \times 10^{14}$ G, a spin-down age $\tau \approx 24.4$ kyr, and a spin-down luminosity $|\dot{E}| \approx 2.4 \times 10^{32}$ erg s^{-1}.

The time-integrated soft X-ray pulse profile of SGR 1830 −0645 initially shows a complex shape, with three prominent peaks, each separated by ≈0.2 cycles. We searched for any temporal evolution by building pulse profiles using observations spanning one to several days, accumulating for each

[30] http://www.cv.nrao.edu/~sransom/presto/

Table 2
SGR 1830−0645 Timing Parameters

Parameter	Value
R.A. (J2000)	18:30:41.64
Decl. (J2000)	−6:45:16.9
Timescale	TDB
Ephemeris	DE405
Epoch (MJD)	59,132.0
ν (Hz)	0.096008680(2)
$\dot{\nu}$ (Hz s^{-1})	$-6.2(1)\times10^{-14}$
$\ddot{\nu}$ (Hz s^{-2})	$4.7(3)\times10^{-21}$
$\dddot{\nu}$ (Hz s^{-3})	$-2.7(4)\times10^{-28}$
Valid range (MJD)	59,132.7–59,355.7
χ^2/dof	177/175
rms residual (ms)	95
Inferred Parameters	
B (G)	2.7×10^{14}
τ (kyr)	24.4
$\lvert\dot{E}\rvert$ (erg s^{-1})	2.4×10^{32}

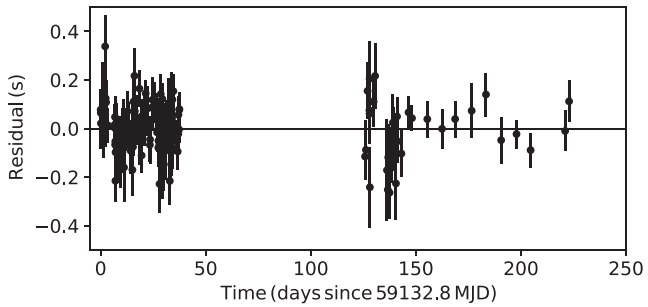

Figure 1. Residuals, in seconds, of a timing model fit to the SGR 1830 −0645 TOAs as derived from 400 to 1200 s of NICER data. The gap constitutes the Sun-constrained period. The model includes up to the fourth term in the Taylor expansion of the phase evolution, and it is summarized in Table 2.

profile an exposure ranging from 4 to 40 ks. The right panel of Figure 2 displays the 0.8–7 keV pulse profiles with 70 phase bins color-coded by time interval in days from MJD 59132.0. The prominent peaks are clearly visible up to day 21 after outburst, after which the profile simplifies to a prominent single peak. However, the fainter peak around a rotational phase of 0.6 remained visible up until the last observation prior to the Sun-constrained period, 37 days after outburst. We note a clear decrease in the separation between the peaks as the outburst evolves. A more detailed analysis of this behavior will be presented elsewhere. The pulse profiles following the Sun-constrained period clearly exhibit a simple broad single-peak pulse.

We also constructed pulse profiles in two energy bands, namely, 0.8–2 keV and 2–7 keV (Figure 2, left and middle panels, respectively). These energy ranges reflect the contribution from the two thermal models necessary to describe the 0.8–7 keV spectrum (see Section 3.3). In both energy ranges, the three peaks are present, and at similar phases. The only subtle distinction in the profiles is the dip between the peaks, where it is more prominent at hard X-rays.

We fit the background-corrected pulse profiles to a Fourier series to measure the rms pulsed fraction (PF_{rms}; Woods et al. 2004). We consider the smallest number of harmonics that provide the best fit to each profile according to an F-test. We find that the first seven harmonics are required to provide an adequate fit to the early pulse shapes. Yet three harmonics are adequate to result in a satisfactory fit to the data after the Sun-constrained period. The source exhibits a highly pulsed signal, with PF_{rms} narrowly varying between 36% and 42% during the first month of the outburst (bottom panel of Figure 3). Subsequent to the Sun-constrained period, the source pulse fraction increased to ≈50%. We find no significant variation in the rms PF with energy.

3.3. Persistent Emission Spectroscopy

We fit the 0.8–7 keV X-ray spectra extracted from all 37 observations taken prior to the Sun-constrained period simultaneously, with an absorbed 2BB model. We link the hydrogen column density among all the spectra since we do not expect any large and variable absorption intrinsic to the magnetar. Initially, we let all other parameters free to vary, i.e., the temperatures and size of the apparent emitting area. We find a reduced χ^2 between 0.9 and 1.1 for all spectra, which have degrees of freedom (dof) ranging from 40 to 440. We observe strong variations in the size of the apparent emitting areas for the warm and hot BB components. The temperatures, on the other hand, remain essentially constant through all observations, varying only at $<2\sigma$ level. Hence, we linked the temperatures of both components between all the spectra and refit the data. This resulted in an equally good fit for all spectra. We find a hydrogen column density in the direction of the source $N_{\rm H}=(1.17\pm0.01)\times10^{22}\,{\rm cm}^{-2}$, while the temperatures of the warm and the hot BB are 0.47 ± 0.01 keV and 1.22 ± 0.01 keV, respectively. We also fit these spectra with the sum of a BB and a power law (PL), affected by interstellar absorption. This model consistently provides a worse fit compared to the 2BB model with χ^2 larger than that of the latter for the same number of dof. This is consistent with the 0.5−30 keV broadband spectral result presented in Coti Zelati et al. (2021), which found that a purely thermal model is the best fit to the soft X-ray part of the spectrum. Hence, for the remainder of the spectral analysis, we adopt the 2BB model.

We then fit the post-Sun-constrained period spectra simultaneously with an absorbed thermal model. We fixed the hydrogen column density to the value as derived above. We find that a single thermal component cannot adequately describe the spectral shape of these spectra, and a 2BB model is still required. We started by allowing the areas and temperatures to vary freely. Once again, the temperatures of all spectra were consistent within uncertainties and, hence, were linked. This final fit resulted in a reduced χ^2 of about 1 for all spectra. The temperatures of the warm and hot BB components are 0.48 ± 0.02 keV and 1.22 ± 0.05 keV, respectively. Figure 4 shows the $EF_{\rm E}$ spectra extracted from a pre- and post-Sun-constrained observation in black and blue, respectively, demonstrating that the flux decay lacks significant spectral shape evolution.

The temporal evolution of the emitting area, R^2, and the absorption-corrected 0.5–10 keV flux of each BB component is shown in Figure 3. Each of these parameters for both BB components follow a similar trend and are well fit with a broken first-order polynomial function (dashed lines). The fits result in χ^2 of 89, 96, 77, and 105 for 59 dof, for the warm and hot areas and corresponding fluxes, respectively. The break occurs shortly after the start of the Sun-constrained period at $t_{\rm break}=46\pm2$ days, or around 2020 November 27. We find a

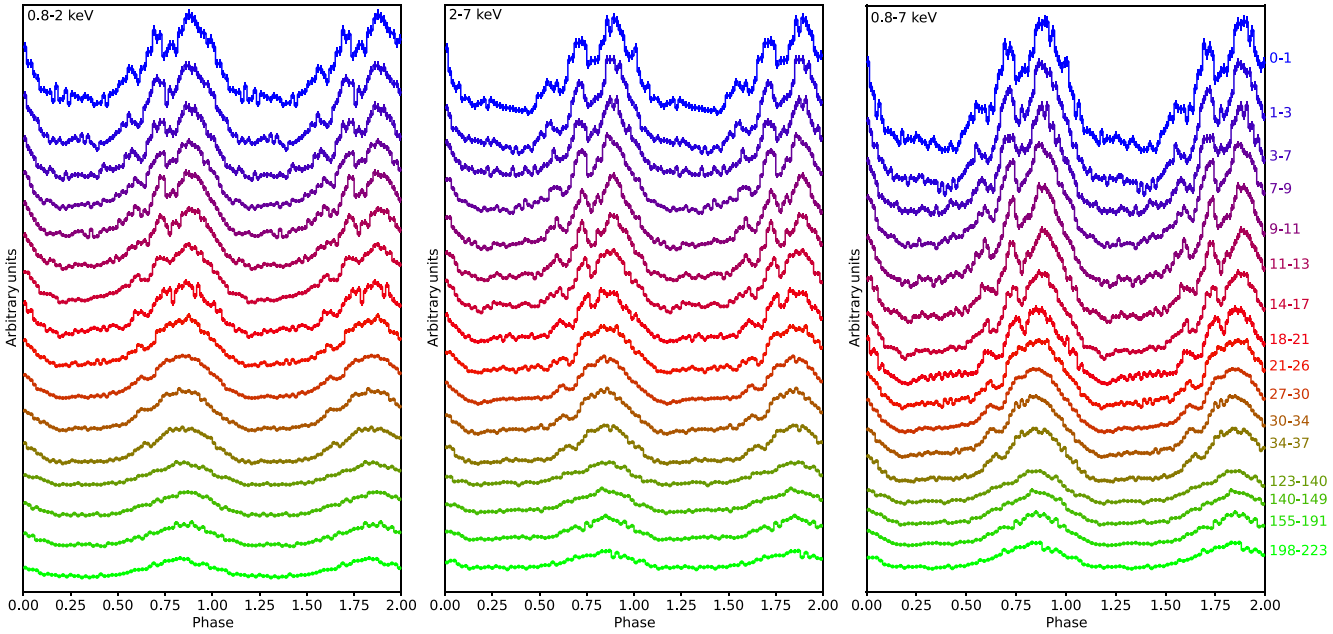

Figure 2. SGR 1830−0645 persistent emission pulse profile evolution with time in the 0.8–2 keV (left panel), 2–7 keV (middle panel), and 0.8–7 keV ranges (right panel). All profiles are corrected for the background. Colors represent the days during which the data are accumulated after 2020 October 10. Two rotational cycles are shown. The *y*-axis is shifted arbitrarily for clarity. See text for more details.

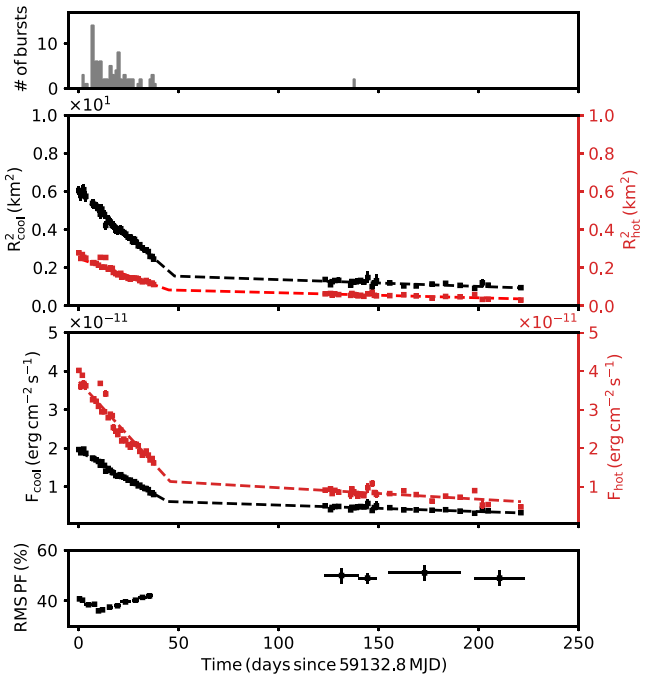

Figure 3. (a) Number of SGR 1830−0645 X-ray bursts per day as observed by NICER. (b) Decay of the hot (red squares) and warm (black squares) BB emitting areas throughout the source outburst. (c) Decay of the absorption-corrected flux of the hot (red squares) and warm (black squares) BB components in the 0.5–10 keV range. In panels (b) and (c) the dotted lines are the best-fit broken-linear decay function. (d) The rms pulsed fraction evolution with time. See text for more details.

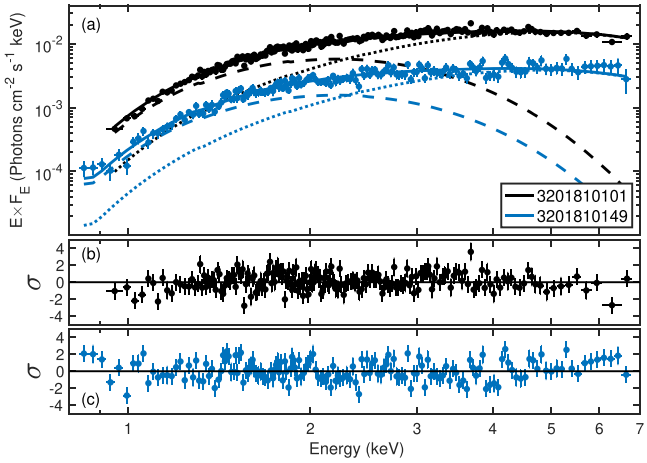

Figure 4. (a) Example NICER spectra from the first observation after outburst (4 hr after the source discovery; black circles) and 138 days later (blue circles). The dashed and dotted lines are the best-fit absorbed warm and hot BB models, respectively, while the solid line is their sum. (b, c) Residuals, in units of standard deviation σ, of each spectrum from the best-fit absorbed 2BB model.

flux decay rate of $-5.7(2)\times10^{-13}$ erg s^{-1} cm^{-2} day^{-1} and $-3.0(5)\times10^{-14}$ erg s^{-1} cm^{-2} day^{-1}, before and after t_{break}, respectively. The ratio of the BB fluxes shows no apparent variation with an average $\langle F_{hot}/F_{warm}\rangle \approx 1.9\pm0.2$. The areas of the hot and warm components shrank from 0.28 to 0.04 km^2 and from 6.0 to 1.0 km^2, respectively.

3.4. X-Ray Bursts

We searched for bursts in the X-ray band with the NICER data sets in the energy range of 0.7–8 keV. We use the Bayesian block technique to search for significant X-ray flux variability in individual event files (Scargle et al. 2013). The blocks with duration shorter than ∼1 s are further examined to exclude those with high backgrounds and multiple blocks in one burst. Moreover, blocks close to the boundaries of a good time interval have also been excluded. The detection significance of a burst is defined through the Poisson probability of detecting a number of photons in a block, given an estimated nonburst count rate calculated from nearby 1 s intervals. We have identified 84 short bursts with Poisson probabilities lower than 2.6×10^{-7}. This corresponds to a

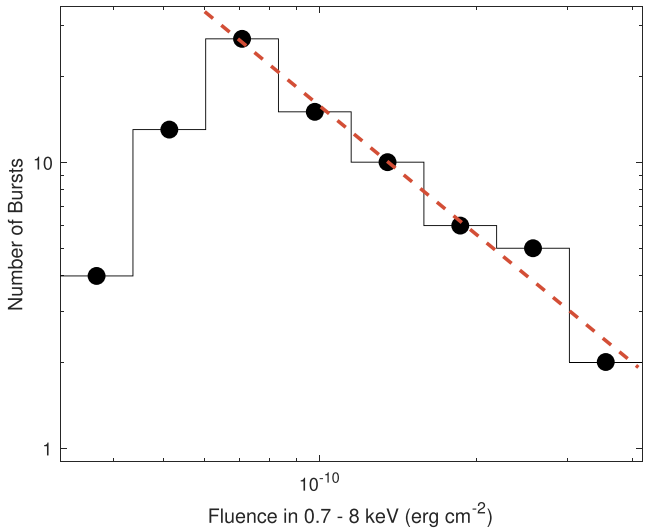

Figure 5. Fluence distribution of bursts in SGR 1830−0645 detected with NICER. For fluences $\gtrsim 6 \times 10^{-11}$ erg cm^{-2}, the distribution approximately follows $F^{-0.5}$, as shown with a red dashed line.

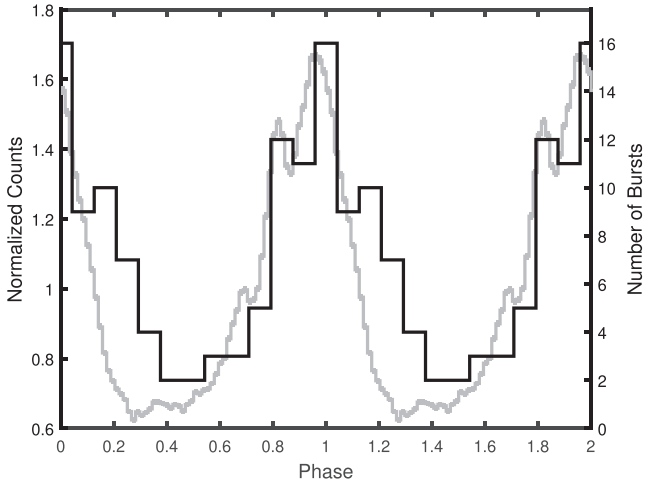

Figure 6. Average pulse profile of SGR 1830−0645 (gray) in the energy range 0.8–7 keV, using all X-ray observations reported in this paper. The black profile represents the histogram of the bursts phase folded using the spin parameters as reported in Table 2.

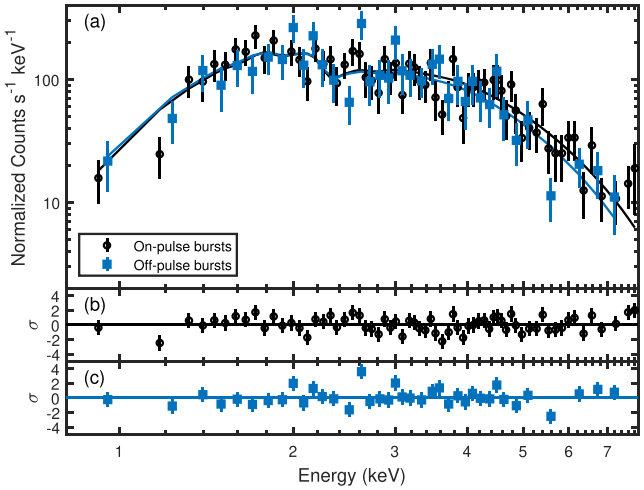

Figure 7. (a) The NICER spectra of the accumulated on-pulse bursts (black circles) and off-pulse bursts (blue squares). The black and blue lines represent the best-fit PL model. (b, c) Residuals of each spectrum from the best-fit PL model in terms of σ.

5.2 σ detection significance and implies a false-alarm rate of $\leqslant 1$ throughout our campaign.

Among the 84 bursts, the averaged Bayesian block duration is about 0.029 s with a standard deviation of 0.023 s. The average photon count rate for the burst ensemble is 470 ± 14 counts s^{-1}, corresponding to an unabsorbed flux of $(4.5 \pm 0.2) \times 10^{-9}$ erg cm^{-2} s^{-1} in the energy range of 0.7–8 keV (assuming a BB with a temperature of 1.5 keV, as derived through our burst spectral analysis below). The burst with the highest fluence occurred at MJD (TDB) 59,139.864807 with a duration of 0.014 s and an average flux of $(3.3 \pm 0.5) \times 10^{-8}$ erg cm^{-2} s^{-1}. The fluence distribution of the bursts is shown in Figure 5. The high-fluence tail, which covers the range (6–30) $\times 10^{-11}$ erg cm^{-2}, can be described by a PL with an index of $\approx$1.5. To estimate the uncertainty of this index, we performed 10^5 simulations. In each, we generated Poisson-distributed photons in each burst with a mean value equal to the observed one, and we calculated the corresponding fluence. The result suggests an uncertainty on the PL index of 0.3.

We investigate the spin-phase distribution of these short bursts using the timing model presented in Table 2. Figure 6 shows the burst-phase distribution along with the pulse profile of SGR 1830−0645 as derived from all observations. It is clear that the burst-phase distribution is not uniform, with its peak occurrence coinciding with the peak of the persistent emission X-ray pulse profile. We apply the Anderson−Darling (AD) test to assess the burst phase against a uniform distribution that yielded an AD statistic of 4.5 with a corresponding p-value of 0.005. Moreover, we performed a simulation to test the significance of this apparent nonuniformity in phase. In each simulation, we generate 83 mock bursts located at randomly distributed spin phases. For 10^5 trials, only $\approx$450 of them result in AD statistics higher than the observed value. This implies that the null hypothesis of the observed burst-phase distribution being drawn from a uniform distribution can be rejected at the 3σ level. Finally, we searched for any phase dependence of the mean photon energy and the fluence of bursts but found no clear trend.

We accumulated a total of 1111 bursts photons in the 0.7–8 keV range. We merged photon events with `nimpumerge` and generated an averaged burst spectrum in the burst time intervals. We fit the spectrum with the Cash statistics (Cash 1979), assuming that the background constitutes the nonburst epochs. We excluded the data sets taken in 2021 owing to the dramatic decrease in the rate of bursting activity. The burst spectrum can be described equally well with an absorbed PL or BB model. We fix the hydrogen column density $N_{\rm H}$ to 1.17×10^{22} cm^{-2} as derived through the persistent emission spectral analysis. We find a photon index of $0.4^{+0.5}_{-0.3}$ ($C_{\rm stat} = 408.5$ with 448 dof) for the PL component, or $kT = 1.5 \pm 0.1$ keV and a radius of 4.1 ± 0.3 km ($C^2 = 362.6$ with 448 dof) when considering the BB model. We further divided bursts into two groups: bursts associated with the X-ray pulse (on-pulse, phase 0.8–1.3) and the X-ray valley (off-pulse, phase 0.3–0.8). No significant difference is obtained between the spectra of these two groups. The on-pulse and off-pulse spectra are shown in Figure 7.

3.5. Radio Upper Limits

Deep Space Network. We dedispersed the S-band and X-band data from DSS-34 with trial dispersion measures (DMs) between 10 and 2000 pc cm^{-3} and independently searched the data in each frequency band for periodic radio emission. We used a GPU-accelerated fast-folding algorithm (FFA) to search for pulsed radio emission with periods between 9 and 12 s. We also used a GPU-accelerated Fourier domain acceleration search (FDAS) pipeline, which employs a matched filtering algorithm to correct for Doppler smearing, to search for periodicity. No statistically significant periods, with a signal-to-noise ratio (S/N) above 7.0, were found after folding the data modulo each of the period candidates identified by the two algorithms. We also folded the data utilizing the NICER ephemerides at the DSN epoch, as well as using trial periods around the predicted 10.42 s rotational period of the source. We do not find any pulsed emission at or near the expected signal. For an assumed duty cycle of 10%, we place the following (7σ) upper limits on the SGR 1830−0645 radio flux density during our radio observation: <0.14 mJy at S band and <0.08 mJy at X band.

We also searched the dedispersed S- and X-band data for radio bursts using a Fourier domain matched filtering algorithm, where each dedispersed time series was convolved with boxcar functions with logarithmically spaced widths between 512 μs and 153.6 ms. Candidates with detection S/Ns above 7.0 were saved and classified using a GPU-accelerated machine-learning pipeline based on the FETCH (Fast Extragalactic Transient Candidate Hunter) software package (Agarwal et al. 2020). The dynamic spectra of the candidates were also visually inspected for verification. No radio bursts were detected above a 7σ fluence detection threshold of 1.8 Jy ms for a 1 ms burst at S band and 1.0 Jy ms for a 1 ms burst at X band.

European stations. We searched the filter banks from each station for single pulses using Heimdall[31] in the DM range 10–2000 pc cm^{-3}. Classification of candidates was performed via FETCH (Agarwal et al. 2020) and manual inspection of the most promising candidates. No attempt of folding the data around the rotational period was done. We found no bursts above an S/N threshold of 7 in any of the observations, constraining the fluence of any potential bursts as summarized in Table 1.

Green Bank Telescope. The data were searched for periodic emission, both completely blind and by folding the data around the known period, and for bright single pulses in the DM range of 10–1500 pc cm^{-3}. We do not detect any significant periodic or single-pulse emission. For periodic emission, we place a 7σ upper limit on the average flux density of 7.8 and 6.2 μJy at S and C band, respectively, assuming a 10% duty cycle. The dedispersed data were also searched for FRBs using Heimdall, and candidates were run through the GPU-accelerated convolutional neural network FETCH (Agarwal et al. 2020) to distinguish between radio frequency interference (RFI) and astrophysical signals. We did not detect any radio bursts in our data, and the 7σ fluence upper limits are 0.07 and 0.04 Jy ms at 2.0 and 6.0 GHz, respectively, assuming a pulse width of 1 ms.

[31] https://sourceforge.net/projects/heimdall-astro/

4. Summary and Discussion

In this paper, we present the results of a NICER heavy-cadence monitoring campaign of the recently discovered magnetar SGR 1830−0645, covering the time interval from 4 hr to 223 days after outburst onset. This dense observing campaign allowed us to track the X-ray spectral and temporal evolution of the source in exquisite detail, while affording an analysis of low-level bursting activity that occurred throughout the outburst. We complement NICER with a Chandra observation that provided the precise sky localization of the source. Finally, we present the results of a suite of SGR 1830−0645 radio observations taken at several frequencies from multiple epochs during the source outburst.

4.1. General Properties

The NICER observations of SGR 1830−0645 allowed us to build an accurate timing solution to the rotational properties of the source over several months. The temporal characteristics we inferred, $\nu = 0.096008680(2)$ Hz and $\dot{\nu} = -6.2(1) \times 10^{-14}$ Hz s^{-1}, are quite typical of the magnetar family, as well as the derived intrinsic properties: $B = 2.7 \times 10^{14}$ G, $\tau = 24.4$ kyr, and $|\dot{E}| = 2.4 \times 10^{32}$ erg s^{-1} (see also Coti Zelati et al. 2021). The long baseline of the observations also revealed the presence of higher-order frequency derivatives, likely indicating a significant level of timing noise (typical of magnetars during outburst epochs; e.g., Younes et al. 2015; Archibald et al. 2020; Hu et al. 2020). All the above properties, along with the strong bursting activity and the persistent flux decay, cement the origin of SGR 1830−0645 as the latest addition to the magnetar family.

The Galactic coordinates of SGR 1830−0645 (Section 3.1) locate this magnetar close to the positions of known magnetars SGR 1833−0832, Swift J1834.9−0846, and 1E 1841−045. These three sources are thought to be on the Galactic Scutum −Centaurus arm (Table 7 and Figure 17 of Enoto et al. 2017). The distances of the latter two sources, Swift J1834.9−0846 and 1E 1841−045, are measured at 4.2 and 8.5 kpc from the associated supernovae remnants (SNRs) W41 (Leahy & Tian 2008) and Kes 73 (Tian & Leahy 2008), respectively. Due to the lack of any SNR around SGR 1830−0645, we assume a fiducial distance of SGR 1830−0645 at 4 kpc as the close part of this spiral arm. The Chandra observation reveals no significant extended emission around the source that may be interpreted as an X-ray wind nebula, in line with the majority of the magnetars (with the exception of Swift J1834.9−0846; Younes et al. 2016).

4.2. X-Ray Evolution during Outburst

The SGR 1830−0645 pulse profile at the onset of the outburst shows a complex morphology, exhibiting three clearly distinct peaks. The initial separation of the peaks is about 0.2 rotational phases, which seem to decrease with time. By day 21 after outburst, the profile simplified to a broad single peak, though the weakest peak around phase 0.65 remained visible until the last observation prior to the Sun-constrained period. Complex profile shapes are quite common for magnetars during their outburst epochs. For instance, the 4U 0142+61 double-peaked profile revealed extra peaks following the source 2006 and 2015 outbursts (Archibald et al. 2017; see also, e.g., Gavriil et al. 2011; Rea et al. 2013). These changes commonly revert back to a simpler shape as the outburst wanes. This is

also the case for SGR 1830−0645, where the pulse profiles following the Sun-constrained period, i.e., 4 months after outburst, evince a single broad pulse.

We find no strong energy dependence on pulse shape, except for a deeper, more pronounced trough between the two main peaks in the energy range 2–7 keV compared to the lower 0.8–2 keV band. Yet these two energy ranges are dominated by each of the two BB components used to fit the 0.8–7 keV phase-averaged spectrum (Figure 4). These two BB components evolve similarly throughout the outburst, i.e., their temperatures remain constant while their areas decrease, driving a very similar flux decay trend (Figure 3). Hence, it is evident that these two spectral components are not distinct. It is plausible that the X-ray-emitting area is not isothermal, but rather possesses a temperature gradient, for example, a hot core surrounded by a cooler ring, which are evolving concurrently. The fact that the hotter component is of slightly higher flux than the cooler one (see Figure 4) provides clues to the concentration of energy deposition in the persistent emission activation zone. The increase of the rms pulse fraction after the Sun-constrained downtime is possibly caused by the lower effective emitting area of both components (e.g., Hu et al. 2020).

The three distinct peaks in the profile at the onset of the outburst clearly indicate an asymmetric, nonuniform heating pattern on the surface, yet with clear evolution toward a simpler, more localized region. In the magnetar model, it is natural to attribute the soft X-ray active regions to being proximate to magnetic field line footpoints on the surface. These footpoints may or may not be associated with dipolar field morphology. Perturbations to this baseline field configuration have been developed in the *twisted field scenario* (e.g., Thompson et al. 2002; Beloborodov 2009), via analogy to solar corona contexts. These introduce toroidal field components driven by inner magnetospheric currents, and it is possible that such magnetospheric field morphology modifications could permeate magnetar atmospheres. Moreover, the currents will naturally bombard the stellar surface (Beloborodov & Li 2016), heating it at the footpoints of twisted field lines. Thus, the hot emission zones may be physically connected to and/or colocated with bombardment footpoints. The pulse phase migration and merging of the peaks seen in Figure 2 as the outburst evolves would suggest hot-spot coalescence and field line footpoint mobility. The rate of pulse profile evolution can potentially constrain twisted field models of magnetar activation, suggesting insightful paths for future studies on the theory/observation interface for magnetars.

Processes that originate in the crust may form an alternate scenario to bombardment by twisted fields for the hot-spot evolution. The rate and character of evolution would be governed by bulk material properties such as viscosity, heat conductivity, and the depth of subsurface energy injection (e.g., Beloborodov & Levin 2014; Lander 2016; Kwang-Hua 2018; Lander & Gourgouliatos 2019). These scenarios will be investigated in a separate study.

4.3. Phase Distribution of Short Bursts

Since our initial observation, NICER frequently detected typical short magnetar bursts from SGR 1830−0645, revealing a total of 84 with an average duration of about 30 ms. Much of the burst activity transpires during the early stages of the outburst evolution, i.e., during the steep flux decline and the strong pulse shape variation (Figures 2 and 3). The fluence was in the range of $(3-30)\times 10^{-11}$ erg cm^{-2}. Brighter bursts have also been detected throughout the outburst by large field of view instruments such as Fermi-GBM and Swift-BAT (Fletcher & Fermi GBM Team 2021; Klingler et al. 2021), though at a much lower rate. This is qualitatively consistent with the steep $\log N$-$\log S$ distribution of the NICER events, $N(>F)\propto F^{-0.5}$. This PL fluence distribution seems to be universal among magnetars (e.g., Cheng et al. 1996; Göğüş et al. 1999; Scholz & Kaspi 2011; Collazzi et al. 2015; Younes et al. 2020a) and may be consistent with either the crust quake or magnetic reconnection scenarios, which are usually invoked as their triggering mechanism (e.g., Thompson & Duncan 1995, 2001; Lyutikov 2003, 2015; Elenbaas et al. 2016).

The apparent phase correlation of the bursts with that of the persistent thermal surface hot-spot emission (Figure 6) is the strongest evidence yet of such phase selection in observability of short bursts in magnetars. Previously, a similar preference for burst occurrence close to the persistent emission pulse maximum has been reported in the radio-emitting magnetar XTE J1810−197, but in a much smaller sample of four bursts (Woods et al. 2005). Observe that this phase variation of burst arrival times contrasts the approximate phase uniformity apparent in the recent burst storm of SGR 1935+2154 (Younes et al. 2020a).

This strong correlation suggests that approximate spatial colocation of bursts and soft X-ray activity is highly likely, with the burst plasma emitting at relatively low altitudes. Given the $R^2\sim 16\,\mathrm{km}^2$ apparent area of the bursts, one expects that occultation of the bursts by the star at some pulse phases is readily achievable. We envisage that the bursts could originate in twisted field line zones near quasi-polar footpoints of closed field lines (Chen & Beloborodov 2017). Polarization-dependent radiative transport in optically thick e^+e^- plasmas in the presence of magnetar-strength B-fields could impart strong beaming of radiation (e.g., Barchas et al. 2021), which could bias observability of bursts at particular phases where the observer samples magnetic field directions roughly parallel to the observer's line of sight. This beaming is strong if the typical NICER-measured burst photon energy of $3kT\sim 3$–5 keV is well below the local cyclotron energy (roughly 2 MeV at the surface): such a domain arises if the altitude of the bursts is less than about 5−7 stellar radii assuming that the local magnetic field is not disrupted. These constraints pose a challenge for reconnection models of magnetar bursts (e.g., those invoking a relativistic tearing instability in an equatorial current sheet; Lyutikov 2003; Komissarov et al. 2007; Elenbaas et al. 2016) and may point to a polar crustal origin (e.g., Lander et al. 2015; Thompson et al. 2017) for the mechanism and locale of these magnetar short bursts. Future polarization studies of magnetar bursts, for instance, with LEAP (McConnell et al. 2017) or AMEGO (McEnery et al. 2019), could elucidate the source geometry and hone in on the altitude and magnetic colatitudes for burst emission.

Finally, since magnetar short bursts could underpin some FRBs (Suvorov & Kokkotas 2019; Wadiasingh & Timokhin 2019; Bochenek et al. 2020; CHIME/FRB Collaboration et al. 2020; Mereghetti et al. 2020), our result of burst-phase dependence has interesting implications for mechanisms, observability, and periodic windowing of extragalactic FRBs, beyond the scope of this paper.

4.4. Radio Behavior

The nondetection of SGR 1830−0645 at MHz and GHz frequencies is commensurate with the majority of magnetar sources. So far, only six magnetars have been detected in the radio band. With the exception of SGR 1935+2154, the properties of the radio emission from magnetars follow a general trend; it is transient, usually appearing during outburst epochs, and the radio spectrum is flat or inverted as opposed to the steep spectrum detected in canonical radio pulsars (e.g., Camilo et al. 2006; Torne et al. 2015; Camilo et al. 2016; Pearlman et al. 2018; Esposito et al. 2020). Yet the radio emission from SGR 1935+2154 is unique to date. Hours after its 2020 April burst storm (Younes et al. 2020a), the source emitted the brightest radio flash ever detected from the Milky Way, with properties reminiscent of extragalactic FRBs (Bochenek et al. 2020; CHIME/FRB Collaboration et al. 2020), simultaneous to a bright, spectrally unique short X-ray burst (Mereghetti et al. 2020; Li et al. 2021; Ridnaia et al. 2021; Tavani et al. 2021; Younes et al. 2021). Many large radio campaigns ensued (weeks of on-source observations); however, only three other radio bursts were detected, with two having fluences between 10 and 100 Jy ms (Kirsten et al. 2021). Our radio observations of SGR 1830−0645 were sensitive to such brightness levels (Table 1). Furthermore, months after SGR 1935+2154 had returned to quiescence, the FAST radio telescope detected very weak pulsed emission from the source (Zhu et al. 2020). Such intermittent radio emission raises the possibility that magnetars may be more prone to low-frequency radiation than is currently thought. Hence, future regular radio monitoring programs of magnetars both in outburst and during quiescent periods may be key to unraveling the nature of the low-frequency emission of these sources and their connection to extragalactic FRBs.

G.Y. is partly funded through the NASA NICER GI program grant 80NSSC21K0233. M.G.B. acknowledges the generous support of the National Science Foundation through grant AST-1813649. Z.W. acknowledges support from the NASA postdoctoral program. Z.W. acknowledges partial support by NASA under award No. 80GSFC21M0002. F.K. acknowledges support from the Swedish Research Council. A.B.P. is a McGill Space Institute (MSI) Fellow and a Fonds de Recherche du Quebec—Nature et Technologies (FRQNT) postdoctoral fellow. C.-P.H. acknowledges support from the Ministry of Science and Technology in Taiwan through grant MOST 109-2112-M-018-009-MY3. This work is based in part on observations carried out using the 32 m radio telescope operated by the Institute of Astronomy of the Nicolaus Copernicus University in Toruń (Poland) and supported by a Polish Ministry of Science and Higher Education SpUB grant. A portion of this research was performed at the Jet Propulsion Laboratory, California Institute of Technology, and the Caltech campus, under a Research and Technology Development grant through a contract with the National Aeronautics and Space Administration. U.S. government sponsorship is acknowledged. W.A.M. thanks the CDSCC staff and the DSN scheduling team for their rapid response in scheduling and carrying out the radio observations with the DSN.

ORCID iDs

George Younes https://orcid.org/0000-0002-7991-028X
Chin-Ping Hu https://orcid.org/0000-0001-8551-2002
Karishma Bansal https://orcid.org/0000-0002-7418-7862
Paul S. Ray https://orcid.org/0000-0002-5297-5278
Aaron B. Pearlman https://orcid.org/0000-0002-8912-0732
Franz Kirsten https://orcid.org/0000-0001-6664-8668
Zorawar Wadiasingh https://orcid.org/0000-0002-9249-0515
Ersin Göğüş https://orcid.org/0000-0002-5274-6790
Matthew G. Baring https://orcid.org/0000-0003-4433-1365
Teruaki Enoto https://orcid.org/0000-0003-1244-3100
Keith C. Gendreau https://orcid.org/0000-0001-7115-2819
Chryssa Kouveliotou https://orcid.org/0000-0003-1443-593X
Tolga Güver https://orcid.org/0000-0002-3531-9842
Alice K. Harding https://orcid.org/0000-0001-6119-859X
Walid A. Majid https://orcid.org/0000-0002-4694-4221
Harsha Blumer https://orcid.org/0000-0003-4046-884X
Jason W. T. Hessels https://orcid.org/0000-0003-2317-1446
Marcin P. Gawroński https://orcid.org/0000-0003-4056-4903
Vladislavs Bezrukovs https://orcid.org/0000-0003-3655-2280

References

Agarwal, D., Aggarwal, K., Burke-Spolaor, S., Lorimer, D. R., & Garver-Daniels, N. 2020, MNRAS, 497, 1661
Archibald, R. F., Kaspi, V. M., Scholz, P., et al. 2017, ApJ, 834, 163
Archibald, R. F., Kaspi, V. M., Tendulkar, S. P., & Scholz, P. 2016, ApJL, 829, L21
Archibald, R. F., Scholz, P., Kaspi, V. M., Tendulkar, S. P., & Beardmore, A. P. 2020, ApJ, 889, 160
Barchas, J. A., Hu, K., & Baring, M. G. 2021, MNRAS, 500, 5369
Beloborodov, A. M. 2009, ApJ, 703, 1044
Beloborodov, A. M., & Levin, Y. 2014, ApJL, 794, L24
Beloborodov, A. M., & Li, X. 2016, ApJ, 833, 261
Bochenek, C. D., Ravi, V., Belov, K. V., et al. 2020, Natur, 587, 59
Camilo, F., Ransom, S. M., Halpern, J. P., et al. 2006, Natur, 442, 892
Camilo, F., Ransom, S. M., Halpern, J. P., et al. 2016, ApJ, 820, 110
Cash, W. 1979, ApJ, 228, 939
Chen, A. Y., & Beloborodov, A. M. 2017, ApJ, 844, 133
Cheng, B., Epstein, R. I., Guyer, R. A., & Young, A. C. 1996, Natur, 382, 518
CHIME/FRB Collaboration, Andersen, B. C., Bandura, K. M., et al. 2020, Natur, 587, 54
Collazzi, A. C., Kouveliotou, C., van der Horst, A. J., et al. 2015, ApJS, 218, 11
Coti Zelati, F., Borghese, A., Israel, G. L., et al. 2021, ApJL, 907, L34
Coti Zelati, F., Rea, N., Pons, J. A., Campana, S., & Esposito, P. 2018, MNRAS, 474, 961
Elenbaas, C., Watts, A. L., Turolla, R., & Heyl, J. S. 2016, MNRAS, 456, 3282
Enoto, T., Shibata, S., Kitaguchi, T., et al. 2017, ApJS, 231, 8
Esposito, P., Rea, N., Borghese, A., et al. 2020, ApJL, 896, L30
Fletcher, C. & Fermi GBM Team 2021, GCN, 29524, 1
Garmire, G. P., Bautz, M. W., Ford, P. G., Nousek, J. A., & Ricker, G. R. J. 2003, Proc. SPIE, 4851, 28
Gavriil, F. P., Dib, R., & Kaspi, V. M. 2011, ApJ, 736, 138
Gavriil, F. P., Gonzalez, M. E., Gotthelf, E. V., et al. 2008, Sci, 319, 1802
Gendreau, K. C., Arzoumanian, Z., Adkins, P. W., et al. 2016, Proc. SPIE, 9905, 99051H
Göğüş, E., Kouveliotou, C., & Younes, G. 2020, ATel, 14085, 1
Göğüş, E., Lin, L., Kaneko, Y., et al. 2016, ApJL, 829, L25
Göğüş, E., Woods, P. M., Kouveliotou, C., et al. 1999, ApJL, 526, L93
Hu, C.-P., Begiçarslan, B., Güver, T., et al. 2020, ApJ, 902, 1
Kaspi, V. M., & Beloborodov, A. 2017, ARA&A, 55, 261
Kirsten, F., Snelders, M. P., Jenkins, M., et al. 2021, NatAs, 5, 414
Klingler, N. J., Lien, A. Y., Page, K. L. & Neil Gehrels Swift Observatory Team 2021, GCN, 29516, 1
Komissarov, S. S., Barkov, M., & Lyutikov, M. 2007, MNRAS, 374, 415
Kouveliotou, C., Dieters, S., Strohmayer, T., et al. 1998, Natur, 393, 235
Kwang-Hua, C. W. 2018, Ap&SS, 363, 184

Lander, S. K. 2016, ApJL, 824, L21
Lander, S. K., Andersson, N., Antonopoulou, D., & Watts, A. L. 2015, MNRAS, 449, 2047
Lander, S. K., & Gourgouliatos, K. N. 2019, MNRAS, 486, 4130
Leahy, D. A., & Tian, W. W. 2008, AJ, 135, 167
Li, C. K., Lin, L., Xiong, S. L., et al. 2021, NatAs, 5, 378
Luo, J., Ransom, S., Demorest, P., et al. 2021, ApJ, 911, 45
Lyutikov, M. 2003, MNRAS, 346, 540
Lyutikov, M. 2015, MNRAS, 447, 1407
Maan, Y., Straal, S., & van Leeuwen, J. 2020, ATel, 14098, 1
Majid, W. A., Pearlman, A. B., Dobreva, T., et al. 2017, ApJL, 834, L2
Majid, W. A., Pearlman, A. B., Nimmo, K., et al. 2020, ApJL, 897, L4
McConnell, M. L., Baring, M. G., Bloser, P. F., et al. 2017, NewAR, 76, 1
McEnery, J., van der Horst, A., Dominguez, A., et al. 2019, BAAS, 51, 245
Mereghetti, S. 2008, A&ARv, 15, 225
Mereghetti, S., Savchenko, V., Ferrigno, C., et al. 2020, ApJL, 898, L29
Page, K. L., Barthelmy, S. D., Klingler, N. J., Kuin, N. P. M., & Lien, A. Y. 2020, ATel, 14083, 1
Pearlman, A. B., Majid, W. A., & Prince, T. A. 2019, AdAst, 2019, 6325183
Pearlman, A. B., Majid, W. A., Prince, T. A., Kocz, J., & Horiuchi, S. 2018, ApJ, 866, 160
Pearlman, A. B., Majid, W. A., Prince, T. A., et al. 2020a, ATel, 14102, 1
Pearlman, A. B., Majid, W. A., Prince, T. A., et al. 2020b, ApJL, 905, L27
Pearlman, A. B., Majid, W. A., Prince, T. A., et al. 2020c, arXiv:2005.08410
Ray, P. S., Kerr, M., Parent, D., et al. 2011, ApJS, 194, 17
Ray, P. S., Younes, G., Guver, T., et al. 2020, ATel, 14112, 1
Rea, N., Borghese, A., Esposito, P., et al. 2016, ApJL, 828, L13
Rea, N., Israel, G. L., Pons, J. A., et al. 2013, ApJ, 770, 65
Remillard, R. A., Loewenstein, M., Steiner, J. F., et al. 2021, arXiv:2105.09901
Ridnaia, A., Svinkin, D., Frederiks, D., et al. 2021, NatAs, 5, 372
Scargle, J. D., Norris, J. P., Jackson, B., & Chiang, J. 2013, ApJ, 764, 167
Scholz, P., & Kaspi, V. M. 2011, ApJ, 739, 94
Surnis, M., Joshi, B. C., Stappers, B., et al. 2020, ATel, 14091, 1
Suvorov, A. G., & Kokkotas, K. D. 2019, MNRAS, 488, 5887
Tavani, M., Casentini, C., Ursi, A., et al. 2021, NatAs, 5, 401
Thompson, C., & Duncan, R. C. 1995, MNRAS, 275, 255
Thompson, C., & Duncan, R. C. 1996, ApJ, 473, 322
Thompson, C., & Duncan, R. C. 2001, ApJ, 561, 980
Thompson, C., Lyutikov, M., & Kulkarni, S. R. 2002, ApJ, 574, 332
Thompson, C., Yang, H., & Ortiz, N. 2017, ApJ, 841, 54
Tian, W. W., & Leahy, D. A. 2008, ApJ, 677, 292
Torne, P., Eatough, R. P., Karuppusamy, R., et al. 2015, MNRAS, 451, L50
Turolla, R., Zane, S., & Watts, A. L. 2015, RPPh, 78, 116901
Viganò, D., Rea, N., Pons, J. A., et al. 2013, MNRAS, 434, 123
Wadiasingh, Z., & Timokhin, A. 2019, ApJ, 879, 4
Whitney, A., Kettenis, M., Phillips, C., & Sekido, M. 2010, in 6th Int. VLBI Service for Geodesy and Astronomy. Proc. 2010 General Meeting, ed. D. Behrend, K. D. Baver et al. (Houston, TX: NASA), 192
Woods, P. M., Kaspi, V. M., Thompson, C., et al. 2004, ApJ, 605, 378
Woods, P. M., Kouveliotou, C., Gavriil, F. P., et al. 2005, ApJ, 629, 985
Younes, G., Baring, M. G., Kouveliotou, C., et al. 2021, NatAs, 5, 408
Younes, G., Güver, T., Kouveliotou, C., et al. 2020a, ApJL, 904, L21
Younes, G., Guver, T., Wadiasingh, Z., et al. 2020b, ATel, 14086, 1
Younes, G., Kouveliotou, C., Kargaltsev, O., et al. 2016, ApJ, 824, 138
Younes, G., Kouveliotou, C., & Kaspi, V. M. 2015, ApJ, 809, 165
Zhu, W., Wang, B., Zhou, D., et al. 2020, ATel, 14084, 1